Modelling gravity-driven film flow on inclined corrugated substrate using a high fidelity weighted residual integral boundary-layer method

Sergii Veremieiev* and Daniel H. Wacks

Department of Engineering, Durham University, Durham, DH1 3LE, UK

*s.veremieiev@durham.ac.uk

Abstract

A computational investigation is conducted concerning the stability of free-surface gravity-driven liquid film flow over periodic corrugated substrate. The underpinning mathematical formulation constitutes an extension of the weighted residual integral boundary-layer (WIBL) method proposed by C. Ruyer-Quil and P. Manneville [Eur. Phys. J. B 15, 357 (2000)] and S.J.D. D'Alessio et al. [Phys. Fluids 21, 062105 (2009)] to include third- and fourth-order terms in the long-wavelength expansion. Steady-state solutions for the free-surface and corresponding curves of neutral disturbances are obtained using Floquet theory and validated against corresponding experimental data and full Navier-Stokes (N-S) solutions. Sinusoidal and smoothed rectangular corrugations with variable steepness are considered. It is shown that the model is capable of predicting characteristic patterns of stability, including short-wave nose and isles of stability/instability as reported experimentally for viscous film flow over inclined topography, providing an attractive trade-off between the accuracy of a full N-S computation and the efficiency of an integral method. The range of parameter values for which the WIBL model remains valid is established, in particular it is shown that its accuracy decreases with Reynolds number and corrugation amplitude, but increases with the steepness parameter and ratio of wavelength to capillary length.

1 Introduction

Gravity-driven liquid film flows over a variety of substrates containing topography play an important role in numerous engineering, biological and medical applications. In the coating industries several devices exist which have been optimised specifically for the continuous production and fast throughput of uniform, defect-free, films on substrates made from plastic, metal, paper, etc [1]. Solar cells are currently manufactured using raw materials that are costly, toxic and scarce (cadmium and gallium). However, using print manufacturing it is possible to produce cells that are exceptionally thin and extremely light-weight, using only a few milligrams

of copper, zinc and tin, thereby substantially reducing both production costs and production times [2]. Other examples of application areas include the manufacture of thin-film transistors [3], organic light-emitting diode displays [4], printed circuits [5], large-area pressure transducers on flexible substrates ("electronic skins") for security, impact monitoring and health diagnostics [6], hydrophilic/hydrophobic coated products and surfaces for water removal [7] or drag reduction [8], tissue engineering and the printing of biologically active materials such as cells, proteins, bacteria and biogels [9].

The dynamics and stability of film flows have attracted considerable attention for several decades as there is a rich variety of internal fluid flow and associated free-surface disturbances observed, see the reviews of [10] and [11]. Flow structures of interest include kinematically or inertially induced eddies in troughs formed by the presence of topography, [12–19], while hydraulic jumps and standing waves [20], caused by both linear [21] and nonlinear [22] resonance of the steady-state free surface, appear.

The issue of the stability of film flow over topographical features has also attracted much attention. The instability of interest takes the form of large-amplitude interfacial waves which are found to propagate with a coherent shape and characteristic speed [23]. The majority of existing studies concerning the stability of film flows rely primarily upon the classical stability condition, originally derived by [24, 25], which predicts that thin films of Newtonian fluids flowing over flat substrates of infinite extent, which are inclined at an angle β to the horizontal, become unstable for Reynolds numbers, $Re > Re_{flat} = (5/4)\cot\beta$. Existing experimental data, however, shows that the presence of surface topography can, under certain conditions, delay the onset of instability, resulting in a higher topography-dependent Re_{crit}. The stabilising and destabilising effects due to topography have been reported for experiments involving rectangular [26] and sinusoidal [27, 28] features. The aforementioned experiments report a slight stabilisation of the respective films compared to the corresponding flow over flat substrate and qualitatively unaffected neutral stability conditions. Subsequent experimental studies [29–33], however, have reported a much more substantial stabilisation of the flow. They conclude that topographies stabilise film flow if the corrugations are sufficiently steep to give rise to a significantly higher average film thickness compared to the corresponding flow over a flat substrate [34]. It has subsequently been suggested that the stabilisation effect is the result of the complex interplay between the underlying eddy structure formed within troughs of the topography and the unsteady free surface disturbance [32, 35].

Theoretical investigations and models for predicting the hydrodynamic stability of thin film flows over topography have been reported in numerous complementary articles [27, 28, 36–42]. One of the most advanced modelling approaches is based on the integral boundary layer (IBL) approximation, namely either Shkadov's non-weighted (NIBL), [42–44], or a modified weighted (WIBL), [38, 45], formulation. This approach relies upon the long-wavelength assumption that places limits on its application for high Reynolds number, capillary number and topography with high amplitude and steepness, such as a rectangular feature. However, it benefits considerably in terms of computational cost compared to a modelling approach based on solution of full Navier-Stokes equations as developed and used by [41, 46]. The WIBL model eliminates

the explicit depth-coordinate dependence from the full N-S system of equations by assuming a parabolic velocity profile and integrating over the depth of the film together with utilising a weighting function, resulting in a set of equations for film thickness and flow rate whose dimensionality is essentially reduced by one. As a result, the WIBL method represents a good trade-off and balance between accuracy and computational efficiency and can be realistically used for three-dimensional topographies. It has been shown that, if the second-order terms are taken into account, the WIBL model is able to capture the leading dynamics and predict the onset and evolution of interfacial instability [38]. In addition, the WIBL model removes the limitations associated with other alternative approaches based on perturbation theory [27], which is limited to corrugations with small amplitude and small substrate inclination angles, and the so-called Benney-type model [40] that is restricted to small long-wave ratios.

Although accurate and computationally efficient relative to other theoretical models, WIBL approach has not yet been reported as able to predict and capture the important experimentally observed short-wave instability modes discussed in [30] or the stability/instability isles revealed in [32, 33, 46]. The proposed aims of the present work is to explore whether such a model based on a weighted residual integral boundary-layer approximation can be further developed that is able to capture experimental and N-S data by predicting free-surface patterns and neutral stability curves including the relevant stabilisation effects of topography. To this end the paper is structured as follows: section 2 provides the necessary mathematical background, with particular emphasis placed on the use of third- and fourth-order WIBL formulations. Section 3 reports and assesses comparisons of the experimental and full N-S results against those generated using the different order WIBL formulations with regard to (i) steady-state free-surface location; (ii) neutral stability charts; (iii) evolution of a sinusoidally-shaped corrugation towards a more rectangularly-shaped one of varying thickness (tip width) by varying the steepness of the topography. Finally, in section 4, the main results are reviewed with appropriate conclusions drawn.

2 Mathematical Background

Consider a two-dimensional laminar film of Newtonian fluid flowing over a regularly-corrugated, inclined surface. The coordinate system (x, z) is oriented such that the x-axis points down the slope, which is inclined at an angle β to the horizontal, the z-axis points in a direction normal to the aforementioned, inclined slope, at time t, as per Figure 1. The solid, corrugated surface is assumed to be periodic and have the following form:

$$s(x) = A \cdot b\left(\frac{2\pi x}{L}\right), \tag{1}$$

where $b(x) \in [0, 1]$ is a normalised periodic function, the exact form of which may vary from case-to-case; A is the corrugation amplitude and L is the corrugation wavelength. The fluid velocity is denoted by $\vec{u} = (u, w)$, the pressure by p, the film thickness by $h(x, t)$ and $f(x, t) =$

$s(x) + h(x,t)$ is the free surface coordinate. The governing equations (i.e. continuity and full Navier-Stokes) are scaled with respect to vertical and horizontal length scales, and associated pressure, velocity and time scales. The vertical length is scaled by the Nusselt film thickness, H, defined as

$$H = \left(\frac{3\mu \dot{V}}{\rho g \sin\beta} \right)^{1/3}, \tag{2}$$

where $\dot{V}$ is the flow rate per unit cross-sectional width, g is accelaration due to gravity, ρ is fluid density and μ is the dynamic viscosity. The horizontal length is scaled by L, velocity by $U = 3\dot{V}/2H$ and pressure by $P = \rho UL/H^2$. Buoyancy and evaporation effects are assumed to be negligible and therefore ignored.

The two-dimensional continuity and Navier-Stokes equations take the following, non-dimensional form

$$\frac{\partial u}{\partial x} + \frac{\partial w}{\partial z} = 0, \tag{3}$$

$$\varepsilon Re \left(\frac{\partial u}{\partial t} + u\frac{\partial u}{\partial x} + w\frac{\partial u}{\partial z} \right) = -\frac{\partial p}{\partial x} + \varepsilon^2 \frac{\partial^2 u}{\partial x^2} + \frac{\partial^2 u}{\partial z^2} + 2, \tag{4}$$

$$\varepsilon^3 Re \left(\frac{\partial w}{\partial t} + u\frac{\partial w}{\partial x} + w\frac{\partial w}{\partial z} \right) = -\frac{\partial p}{\partial z} + \varepsilon^4 \frac{\partial^2 w}{\partial x^2} + \varepsilon^2 \frac{\partial^2 w}{\partial z^2} - 2\varepsilon \cot\beta, \tag{5}$$

where $\varepsilon = H/L$ is the shallowness parameter (also long-wavelength parameter) and $Re = \rho UH/\mu$ is the Reynolds number. Equations (3-5) are subject to the following dynamic boundary conditions at the free surface [47]

$$p = \frac{2\varepsilon^2}{(1+\varepsilon^2 g)} \left[\varepsilon^2 g \frac{\partial u}{\partial x} + \frac{\partial w}{\partial z} - \frac{\partial f}{\partial x}\frac{\partial u}{\partial z} - \varepsilon^2 \frac{\partial f}{\partial x}\frac{\partial w}{\partial x} \right] - \frac{\varepsilon^3}{Ca\,(1+\varepsilon^2 g)^{3/2}} \frac{\partial^2 f}{\partial x^2} \quad \text{at} \quad z = f, \tag{6}$$

$$\frac{\partial u}{\partial z} + \varepsilon^2 \frac{\partial w}{\partial x} = \frac{4\varepsilon^2}{(1-\varepsilon^2 g)} \frac{\partial f}{\partial x}\frac{\partial u}{\partial x} \quad \text{at} \quad z = f, \tag{7}$$

where $g(x,t) = \left(\frac{\partial f}{\partial x}\right)^2$ is the curvature prefactor, $Ca = \mu U/\gamma$ is the capillary number and γ is the fluid surface tension. By making use of equations (3) and (7) the boundary condition for pressure, (6), is expressed

$$p = -\frac{2\varepsilon^2 (1+\varepsilon^2 g)}{(1-\varepsilon^2 g)} \frac{\partial u}{\partial x} - \frac{\varepsilon^3}{Ca\,(1+\varepsilon^2 g)^{3/2}} \frac{\partial^2 f}{\partial x^2} \quad \text{at} \quad z = f. \tag{8}$$

The kinematic condition describing the position of the free surface is given by

$$w = \frac{\partial f}{\partial t} + u\frac{\partial f}{\partial x} \quad \text{at} \quad z = f. \tag{9}$$

The no-slip and impermeability conditions at the corrugated substrate are satisfied by setting

the tangential and normal fluid velocity components to zero

$$u = w = 0 \text{ at } z = s, \tag{10}$$

where the scaled substrate profile is given by

$$s(x) = \frac{A}{H} \cdot b\left(2\pi x\right). \tag{11}$$

Averaging the equations over the depth of the flow removes the z-dependence, yielding a one-dimensional set of equations. Integrating the continuity equation (3) with the kinematic (9) and no-slip (10) boundary conditions gives

$$\frac{\partial h}{\partial t} + \frac{\partial q}{\partial x} = 0, \tag{12}$$

where q is the flow rate given by

$$q = \int_s^f u dz. \tag{13}$$

Integrating (5) from $z = f$ to $z = z$, using the continuity equation (3) and substituting the value for the pressure at the free surface from (8) provides the following expression for the fluid pressure

$$\begin{aligned} p = 2\varepsilon \cot\beta\left(f - z\right) - \varepsilon^2\left(\frac{\partial u}{\partial x} + \frac{(1+3\varepsilon^2 g)}{(1-\varepsilon^2 g)}\frac{\partial u}{\partial x}\Big|_{z=f}\right) - \frac{\varepsilon^3}{Ca\left(1+\varepsilon^2 g\right)^{3/2}}\frac{\partial^2 f}{\partial x^2} \\ +\varepsilon^3 Re\int_z^f\left(\frac{\partial w}{\partial t} + u\frac{\partial w}{\partial x} + w\frac{\partial w}{\partial z}\right)dz - \varepsilon^4\int_z^f \frac{\partial^2 w}{\partial x^2}dz, \end{aligned} \tag{14}$$

which can be used to eliminate the pressure from the x-momentum equation (4). Following [38, 45], the WIBL technique is implemented to eliminate the z-dependence by firstly assuming the following self-similar parabolic velocity profile across film:

$$u = \frac{3q}{2h^3}(z - s)(2h - z + s). \tag{15}$$

Note that the assumed profile for the velocity satisfies the no-slip condition (10) and zero-order shear condition (7), namely $\partial u/\partial z = 0$ at $z = f$, and represents the steady and uniform flow. The profile $(z-s)(2h-z+s)$ is taken as the weighting function; multiplying (4) by this function and integrating with respect to z from s to f by making use of shear condition (7) and equation (12) results in the desired dimensionless system of equations. These include the continuity-type equation (12) and momentum equation (A.1) obtained using *Maple* and provided in full in Appendix A. Solutions to different order of accuracy, i.e. first, second, third and fourth order, are referred to subsequently as WIBL1, WIBL2, WIBL3 and WIBL4, respectively. Note the WIBL1-2 models are equivalent to the first- and second-order modified models originally derived for flow over flat substrate in [45] and later extended to incorporate the effect of topography in [38]. The WIBL3 model includes extra terms originating from w-inertia in equation (14),

while WIBL4 one includes all the high-order terms consistent with the full two-dimensional N-S system of equations. Even though WIBL4 model, which is based on parabolic profile, is able to capture the free-surface profiles reasonably well, when the free-surface is pronounced for large β or small d WIBL4 is not able to predict the fourth-order curvature prefactor g enough accurately, therefore it is consistently ignored in all our calculations by setting $g = 0$.

In order to investigate how small perturbations $\hat{h}$ and $\hat{q}$ evolve over time, superimposing them with the steady-state solutions h_s and q_s gives:

$$\begin{aligned} h &= h_s(x) + \hat{h}(x,t), \\ q &= q_s(x) + \hat{q}(x,t). \end{aligned} \tag{16}$$

Equation (12) implies that the steady-state solution for q is a constant, since $\dfrac{\partial q}{\partial x} = 0$, therefore $q_s = \dot{V}/UH = 2/3$. Accordingly $h_s(x)$ is determined by solving the steady-state equation (B.1) given in Appendix B. Substituting (16) into governing equations (12) and (A.1) and linearising over small perturbations one obtaines

$$\begin{cases} \dfrac{\partial \hat{h}}{\partial t} + \dfrac{\partial \hat{q}}{\partial x} = 0, \\ \displaystyle\sum_{k=0}^{k=2} \alpha_k(x) \frac{\partial^{k+1} \hat{q}}{\partial t \partial x^k} + \sum_{k=0}^{k=4} \left[\beta_k(x) \frac{\partial^k \hat{h}}{\partial x^k} + \gamma_k(x) \frac{\partial^k \hat{q}}{\partial x^k} \right] = 0, \end{cases} \tag{17}$$

where $\alpha_k(x)$, $\beta_k(x)$ and $\gamma_k(x)$ are periodic coefficients given by equations (C.1 - C.3) of Appendix C. Since the substrate is a periodic function these are also periodic. Applying Floquet theory for the stability analysis leads to

$$\begin{aligned} \hat{h} &= e^{\sigma t} e^{2\pi i Q x} \sum_{m=-F}^{m=F} \hat{h}_m e^{2\pi i m x}, \\ \hat{q} &= e^{\sigma t} e^{2\pi i Q x} \sum_{m=-F}^{m=F} \hat{q}_m e^{2\pi i m x}, \end{aligned} \tag{18}$$

where $Q \in [0,1]$ is the Floquet parameter, F is the number of Floquet harmonics, $\Re(\sigma)$ is the temporal growth rate and $\Im(\sigma)$ is the circular frequency. The problem reduces to the generalised eigenvalue problem $(\sigma A - B)\,\hat{x} = 0$, $\hat{x} = \left(\hat{h}_m, \hat{q}_m\right)^T$ as follows

$$\begin{cases} \sigma \hat{h}_n + 2\pi i\,(Q+n)\,\hat{q}_n = 0 \qquad \text{for } \; n = -F \,..\, F, \\ \displaystyle\sum_{m=-F}^{m=F} \sigma \sum_{k=0}^{k=2} (2\pi i)^k\,(Q+m)^k\,\alpha_{k,n-m} \hat{q}_m + \sum_{k=0}^{k=4} (2\pi i)^k\,(Q+m)^k \left(\beta_{k,n-m} \hat{h}_m + \gamma_{k,n-m} \hat{q}_m \right) = 0, \end{cases} \tag{19}$$

where $\alpha_{k,n-m} = \int_0^1 \alpha_k(x) e^{-2\pi i (n-m) x} dx$, $\beta_{k,n-m} = \int_0^1 \beta_k(x) e^{-2\pi i (n-m) x} dx$ and $\gamma_{k,n-m} = \int_0^1 \gamma_k(x) e^{-2\pi i (n-m) x} dx$ are the Fourier expansion coefficients. Matrices A and B are of order $[2(2F+1), 2(2F+1)]$ and are computed numerically together with eigenvalues de-

termined using Matlab's built-in subroutine *eig*. Since there is symmetry $\sigma_n(-Q) = \sigma_n^*(Q)$ and periodicity $\sigma_n(1+Q) = \sigma_n(Q)$ there is, therefore, also symmetry $\sigma_n(1-Q) = \sigma_n^*(Q)$ and $\sigma_n(0.5+Q) = \sigma_n^*(0.5-Q)$ for $n = 1, ..., 2(2F+1)$, and it is sufficient to consider values of the Floquet parameter Q only from half of its original interval, $Q \in [0, 0.5]$, see also [46] for further details. Here the superscript * denotes complex conjugation. In the spectrum of the stability problem all $2(2F+1)$ eigenvalues are considered. The eigenvalue with the maximum real part defines the stability.

The problem consists of five independent parameters, namely Re, β, Ca, ε, A/H and the function $b(x)$ describing the wall configuration. Following [46] a different set of five independent parameters can also be considered, namely Re, β, Kapitza number $Ka = \left(\frac{\rho\gamma^3}{g\mu^4}\right)^{1/11} = \left(\frac{\sin\beta Re^2}{2Ca^3}\right)^{1/11}$, scaled wavelength $L/L_c = \frac{\sqrt{2Ca/\sin\beta}}{\varepsilon}$ (that measures wavelength in terms of static capillary length $L_c = \sqrt{\gamma/\rho g}$) and scaled amplitude $A/L = \varepsilon \cdot A/H$ (that measures amplitude in terms of wavelength). A smooth periodic rectangular corrugation is defined via the wall shape function $b(x)$:

$$b_1(x) = \begin{cases} \cos\left(\pi\dfrac{x+0.5-w}{1-w}\right), & |x-0.5| \le 1-w \text{ and } w \ge 0.5, \\ 1, & |x-0.5| \ge 1-w \text{ and } w > 0.5, \\ \cos\left(\pi\dfrac{|x-0.5|-0.5}{w}\right), & |x-0.5| > 0.5-w \text{ and } w < 0.5, \\ -1, & |x-0.5| \le 0.5-w \text{ and } w < 0.5, \end{cases} \tag{20}$$

$$b(x) = 0.5\left[1 + \text{sign}\left(b_1(x)\right) \cdot |b_1(x)|^d\right], \tag{21}$$

introducing two more independent parameters, namely the dimensionless tip width $w = W/L \in [0, 1]$ and steepness parameter $d \in [0, 1]$ of the wall corrugation. It is easy to see that $d = 1$ and $w = 0.5$ correspond to a perfectly sinusoidal wall shape, while decreasing steepness to the smallest value $d = 0$ results in a perfectly rectangular profile, as per Fig. 2(a), allowing the effect of steepness to be considered. This can also be combined with the effect of tip width, as per Fig. 2(b).

3 Results and Discussion

Steady-state solutions for films flowing over substrate having a sinusoidal profile for cases reported elsewhere in the literature are considered first. Matlab's built-in function *fsolve* is used to obtain steady-states with residuals reduced below 10^{-6}; WIBL models of up to fourth-order accuracy are considered as per Appendix B with the steady-state prefactor taken as $g_s = 0$.

Fig. 3(a-c) shows the effect of Re on steady-state free surface shape for small $L/L_c = 1.057$ and amplitude $A/L = 0.2$. The WIBL1-4 models are seen to be in excellent agreement with

each other and the N-S solutions from Fig. 5 of [17] for Re up to 22.5; even WIBL1 is good enough in this case. Fig. 3(d-g) reveals the corresponding results for moderate $L/L_c = 3.342$ and amplitude $A/L = 0.2$. In this case the WIBL2-4 models are found to be in reasonably good agreement with each other and the N-S solutions from Fig. 6 of [17] for Re up to 22.5; the discrepancy between the models increases with increasing Re as the free surface becomes more pronounced. WIBL1 noticeably returns the least satisfactory solution for the Re range considered.

The corresponding Fig. 4(a-d) reveals the effect of amplitude A/L on the steady-state free surface profile for $Re = 12.75$ and large $L/L_c = 13.746$. Good agreement between WIBL3 & WIBL4 for A/L up to 0.2 is achieved with the discrepancy between the models getting larger with increasing A/L. For $A/L = 0.4$ WIBL4 provides good qualitative agreement with the N-S solution from Fig. 9 of [41]; WIBL1-3 underperform with WIBL3 being the closer of the three but exhibiting an unphysical bump on the free-surface. On increasing the Re to 17.55, Fig. 4(e-h), the discrepancy between the WIBL1-4 models becomes larger; a similar but less pronounced effect of the Re is observed in Fig. 3 for moderate L/L_c. The increased discrepancy is because the Kapitza number is fixed at $Ka = 1.434$ and the shallowness parameter ε increases with Re (according to the relationship $\varepsilon = \dfrac{(2Re/\sin\beta)^{1/3}}{Ka^{11/6} \cdot L/L_c}$) from 0.278 for $Re = 12.75$ to 0.366 for $Re = 17.55$ stretching the limit of long-wavelength approximation.

Fig. 5 explores the effect of smaller Kapitza number $Ka = 1.069$ on the steady-state free surface profile for $Re = 7.0$ and 16.0. Those obtained by WIBL1-4 are less pronounced than for the case $Ka = 1.434$ and are compared to the experimental curves from Fig. 8 of [35]. Good agreement between WIBL3 & WIBL4 and the experimental data is achieved for A/L up to 0.2; however, the discrepancy gets larger with increasing A/L and Re, with WIBL1 & WIBL2 noticeably underperforming.

Curves of neutral stability produced for films flowing over a sinusoidally varying substrate available in the literature are now considered. Matlab's built-in function *contour* is used to obtain contours of $\Re(\sigma) = 0$. The WIBL models for linearised perturbation equations (17) of up to fourth-order accuracy are considered with the coefficients provided in Appendix C and the steady-state prefactor taken as $g_s = 0$. Fig. 6 shows the effect of the number of Floquet harmonics F on the curves of neutral disturbance obtained by WIBL2 for the case considered in Fig. 1 of [42] with small amplitudes $A/L = 0.01, 0.02, 0.04, 0.08$; [42] employed a first-order non-weighted model that, as expected, for such low amplitudes has very good agreement with WIBL2. However it predicts $Re_{flat} = \cot\beta$, and as such for comparison purpose the neutral stability curves are presented in terms of Re/Re_{flat}. Noted that for $A/L = 0.01$, $F = 1$ is sufficient to produce an F-independent neutral stability chart, which then increases to F=2, 4 and 7 for $A/L = 0.02, 0.04$ and 0.08, respectively. $F = 10$ is used subsequently for obtaining computational results.

Fig. 7(a-d) considers the effect of amplitude A/L on curves of neutral disturbance obtained by WIBL1-4 for the case considered in Fig. 3a of [41] for $Ka = 1.434$ and large $L/L_c = 13.746$. Similar to the steady-state free-surface profiles, good agreement between WIBL3 &

WIBL4 and the N-S solution for A/L up to 0.2 is achieved, with the discrepancy between the models becoming larger with increasing A/L. WIBL2 is able to capture the main features of the neutral stability curve for small amplitudes up to $A/L = 0.1$ only, while WIBL1 greatly underperforms for all A/L. WIBL4 provides good qualitative agreement to the N-S solution from [41] for $A/L = 0.4$ by capturing the short-wave nose present, however it overpredicts its critical Reylnolds number Re_{crit} by about 30%. Fig. 7(e-h) shows the effect of amplitude A/L for a smaller Kapitza number $Ka = 1.069$ as considered in Fig. 3a' of [41]. For $A/L \leq 0.1$ WIBL3 & WIBL4 are seen to be in excellent quantitative agreement with the corresponding N-S solution. For $A/L \geq 0.2$ the performance of the WIBL models is poorer, with only WIBL4 having qualitatively good agreement with the N-S solution and capable of capturing the isles of stability and instability; however, the characteristic Re_{crit} is about 10-40% larger as revealed in the graphical extended inserts provided, while WIBL1-3 significantly underperforms in predicting the associated stability charts.

The effect of inclination angle on curves of neutral disturbance is explored in Fig. 8 for moderate $L/L_c = 4.982$ and $Ka = 3.604$. Agreement with the N-S solution from Fig. 8c of [46] is excellent for WIBL2-4 for large $\beta \geq 10^\circ$, as all models predict the short-wave nose that was originally reported in [30] very well. WIBL1 is observed to significantly underperform for the range of inclination angles considered. Fig. 9 shows the effect of L/L_c on curves of neutral disturbance for moderate $Ka = 3.604$ and $\beta = 10^\circ$. It is noted that agreement with the N-S solution from Fig. 9a of [46] is excellent for the WIBL2-4 models, while WIBL1 significantly underperforms for the considered range of L/L_c.

Fig. 10 considers Q_{crit} and Re_{crit}/Re_{flat} for the short-wave instability presented in Fig. 8 with $L/L_c = 4.982$ and $Ka = 3.604$. The results of the WIBL1-4 models are compared with the experimental data from Figs. 10 and 12 of [30] and the N-S solution from Fig. 8d of [46]; for consistency Variant1b is presented that corresponds to the maximum growth rate from all $2(2F + 1)$ eigenvalues. Experimental Q_{crit} is obtained from the wavelength of the short-wave mode at inception as $\min(L/L_{crit}, 1 - L/L_{crit})$ and comparison with WIBL2-4 is excellent in particular for large β showing the decrease in Q_{crit} in the range $\beta \in [10^\circ, 45^\circ]$. Comparison of Re_{crit}/Re_{flat} is quantitatively good for WIBL2-4 showing a monotonous increase in Re_{crit}/Re_{flat} in the range $\beta \in [10^\circ, 45^\circ]$. WIBL2-4 underperform for $\beta = 5^\circ$, while WIBL1 significantly underperforms for the entire range of β.

The focus is now shifted to the curves of neutral disturbances produced for films flowing over smoothed rectangular corrugations, the investigation is motivated by corresponding experimental data obtained for rectangular corrugation in Fig. 15 of [33] that reveals a strong effect of tip width of the corrugation w on the short-wave instability which appears for $w = 0.5$ and becomes strongly pronounced as w is decreased to 0.025. The experimental result was obtained for $A/L = 0.2$, however here the amplitude is decreased to $A/L = 0.1$ to stay within the limit of long-wavelength approximation.

Fig. 11 shows the effect of the steepness parameter d on curves of neutral disturbance obtained by WIBL3-4 for $w = 0.5$, $Ka = 1.223$ and large $L/L_c = 27.446$. Firstly, the discrepancy between the WIBL3 and WIBL4 results becomes larger as steepness is decreased from $d = 1.0$

to $d = 0.5$, indicating that the accuracy of the WIBL model is sensitive to this parameter. Secondly, WIBL4 is capable of predicting the nose of the short-wave instability observed in the experiments of [33] for rectangular corrugations: the nose is present for $d = 1.0$, it is more pronounced for $d = 0.6$ and finally it decreases in size and shape for $d = 0.5$. Therefore the steepness value $d = 0.6$ was chosen as optimal for further investigation of the effect of corrugation tip width.

The effect of corrugation tip width w on curves of neutral disturbance obtained by WIBL3-4 for $d = 0.6$, $Ka = 1.223$ and large $L/L_c = 27.446$ is demonstrated in Fig. 12. Firstly, the discrepancy between WIBL3 and WIBL4 becomes larger when w is decreased from 0.5 to 0.3 as well as when increased from 0.5 to 0.7. This indicates that the WIBL models are not only limited by $A/L \ll 1$, but also by $A/\min(W, L-W) \ll 1$, the latter is the characterisitic lengthscale for rectangular topography, and as the tip width W gets smaller or larger compared to $L/2$ the long-wavelength approximation and parabolic velocity profile become less applicable. Secondly, WIBL4 is able to capture the nose of the short-wave instability and predict its shape as w changes becoming narrower and sharper as w is decreased from 0.5 to 0.3, while fully disappearing as w is increased from 0.5 to 0.7.

4 Conclusions

A theoretical model is presented for exploring gravity-driven free-surface film flow over periodically repeating corrugated substrate and prediction of the conditions leading to the onset of free-surface instability. The model successfully extends the standard first and second-order accurate weighted residual integral boundary-layer (WIBL1-2) method to include third- and fourth-order terms in the long-wavelength expansion, namely WIBL3-4. Steady-state solutions for the free-surface and linear stability analysis based on Floquet theory are presented and compared against those from experiments and full Navier-Stokes solutions. Both sinusoidal and smoothed rectangular corrugations with variable steepness are considered.

The key findings from this investigation are comprised of the following. It is shown that the model is capable of predicting characteristic patterns of free-surface disturbance and neutral stability curves, including short-wave nose and isles of stability/instability as reported in experiments for gravity-driven viscous film flow over inclined substrate containing topography. The WIBL models consists of a trade-off between the accuracy of a full Navier-Stokes computation and the efficiency of an integral method, therefore presenting a potential attractive means of extension and utilisation for understanding free-surface film flows over three-dimensional topographies where the computational times involved remain prohibitively restrictive.

The limitations of WIBL models of different orders of accuracy for a range of the parameter values of interest are also established. In particular, it is shown that the discrepancies between the WIBL1-4 models grow with Reynolds number Re, relative amplitude A/L, scaled wavelength L/L_c, steepness d and the tip width w of the corrugation. As expected the WIBL4 model is found to be the most accurate and suitable for analysing the stability of liquid film flow over topography. For sinusoidal topography it is found to provide quantitatively good agreement

with corresponding N-S solutions for Reynolds numbers up to $Re = 20$ and amplitudes up to $A/L = 0.2$ with steepness $d = 1.0$. However, the range of amplitudes for which the WIBL4 model is applicable decreases as the value of the steepness parameter is reduced; for example for $d = 0.6$ reasonably good results are produced for amplitudes up to $A/L = 0.1$ only. It is also shown that the best agreement with the N-S solutions is achieved for small and moderate L/L_c and large inclination angles $\beta \geq 10°$. As to further work, an obvious improvement would be to the assumption and use of a parabolic velocity profile, (15), to derive the WIBL equations and as an associated weighting.

Acknowledgements

SV gratefully acknowledges the financial support of EPSRC first grant EP/P011071/1 in enabling the research. Both authors wish to thank Prof P.H. Gaskell for his many insightful suggestions and comments during the course of the work.

Appendix A Time-Dependent WIBL1-4 Models

Each individual model is obtained by cancelling terms of higher order.

$$
\begin{aligned}
&\varepsilon Re\left(\frac{\partial q}{\partial t}+\frac{17q}{7h}\frac{\partial q}{\partial x}-\frac{9q^2}{7h^2}\frac{\partial h}{\partial x}\right)=\frac{5h}{3}-\frac{5q}{2h^2}-\frac{5h\varepsilon\cot\beta}{3}\frac{\partial f}{\partial x}+\frac{5h\varepsilon^3}{6Ca}\frac{\partial}{\partial x}\Big[\frac{1}{(1+\varepsilon^2 g)^{3/2}}\frac{\partial^2 f}{\partial x^2}\Big]\\
&+\varepsilon^2\Big[\frac{9}{2}\frac{\partial^2 q}{\partial x^2}-\frac{6q}{h}\frac{\partial^2 h}{\partial x^2}-\frac{15qs''}{4h}-\frac{9}{2h}\frac{\partial h}{\partial x}\frac{\partial q}{\partial x}+\frac{4q}{h^2}\left(\frac{\partial h}{\partial x}\right)^2-\frac{5qs'}{2h^2}\frac{\partial h}{\partial x}-\frac{5q\left(s'\right)^2}{h^2}\Big]\\
&+\varepsilon^3 Re\Big[-\frac{29}{56}\left(\frac{\partial h}{\partial x}\right)^2\frac{\partial q}{\partial t}-\frac{115q^2}{672h^2}\left(\frac{\partial h}{\partial x}\right)^3-\frac{1205q^2}{2688}\frac{\partial^3 h}{\partial x^3}-\frac{73q^2 s'''}{128}+\frac{163q^2 s'}{224h^2}\left(\frac{\partial h}{\partial x}\right)^2\\
&\quad+\frac{11h^2}{56}\frac{\partial^3 q}{\partial x^2\partial t}-\frac{277qs''}{128}\frac{\partial q}{\partial x}+\frac{15qs'}{64}\frac{\partial^2 q}{\partial x^2}-\frac{9q^2 s's''}{7h}-\frac{163q^2 s'}{448h}\frac{\partial^2 h}{\partial x^2}+\frac{9q^2\left(s'\right)^2}{7h^2}\frac{\partial h}{\partial x}\\
&\quad+\frac{253q}{672h}\frac{\partial q}{\partial x}\left(\frac{\partial h}{\partial x}\right)^2+\frac{555q^2}{896h}\frac{\partial^2 h}{\partial x^2}\frac{\partial h}{\partial x}-\frac{17q\left(s'\right)^2}{7h}\frac{\partial q}{\partial x}-\frac{509}{672}\left(\frac{\partial q}{\partial x}\right)^2\frac{\partial h}{\partial x}-\frac{\partial q}{\partial t}\left(s'\right)^2\\
&\quad-\frac{107h}{336}\frac{\partial^2 h}{\partial x^2}\frac{\partial q}{\partial t}-\frac{5hs''}{12}\frac{\partial q}{\partial t}+\frac{11h}{56}\frac{\partial h}{\partial x}\frac{\partial^2 q}{\partial x\partial t}+\frac{683h}{1008}\frac{\partial q}{\partial x}\frac{\partial^2 q}{\partial x^2}+\frac{601hq}{1008}\frac{\partial^3 q}{\partial x^3}-\frac{29s'}{32}\left(\frac{\partial q}{\partial x}\right)^2\\
&\quad-\frac{11s'}{8}\frac{\partial h}{\partial x}\frac{\partial q}{\partial t}-\frac{4633q}{2688}\frac{\partial^2 h}{\partial x^2}\frac{\partial q}{\partial x}+\frac{187q}{1344}\frac{\partial h}{\partial x}\frac{\partial^2 q}{\partial x^2}+\frac{185q^2 s''}{896h}\frac{\partial h}{\partial x}-\frac{297qs'}{224h}\frac{\partial q}{\partial x}\frac{\partial h}{\partial x}\Big]\\
&+\varepsilon^4\Big[\frac{33q}{7h}\left(\frac{\partial h}{\partial x}\right)^2\frac{\partial^2 h}{\partial x^2}-3s'\frac{\partial q}{\partial x}\frac{\partial^2 h}{\partial x^2}-\frac{5q}{7h^2}\left(\frac{\partial h}{\partial x}\right)^4-\frac{15\left(s'\right)^3}{4h}\frac{\partial q}{\partial x}-\frac{5q\left(s'\right)^4}{2h^2}\\
&\quad+\frac{9}{14h}\left(\frac{\partial h}{\partial x}\right)^3\frac{\partial q}{\partial x}-\frac{9s'}{2h}\left(\frac{\partial h}{\partial x}\right)^2\frac{\partial q}{\partial x}-\frac{39\left(s'\right)^2}{4h}\frac{\partial h}{\partial x}\frac{\partial q}{\partial x}-\frac{27qs''}{8}\frac{\partial^2 h}{\partial x^2}+\frac{3s'}{4}\frac{\partial h}{\partial x}\frac{\partial^2 q}{\partial x^2}\\
&\quad-\frac{47q}{28}\frac{\partial h}{\partial x}\frac{\partial^3 h}{\partial x^3}+\frac{5q\left(s'\right)^3}{4h^2}\frac{\partial h}{\partial x}+\frac{33q\left(s'\right)^2}{4h^2}\left(\frac{\partial h}{\partial x}\right)^2-\frac{45q\left(s'\right)^2 s''}{8h}+\frac{4qs'}{h^2}\left(\frac{\partial h}{\partial x}\right)^3\\
&\quad-\frac{39q\left(s'\right)^2}{8h}\frac{\partial^2 h}{\partial x^2}-\frac{141}{28}\frac{\partial h}{\partial x}\frac{\partial q}{\partial x}\frac{\partial^2 h}{\partial x^2}-\frac{6qs's''}{h}\frac{\partial h}{\partial x}-\frac{3qs'}{4h}\frac{\partial h}{\partial x}\frac{\partial^2 h}{\partial x^2}+\frac{3qs''}{2h}\left(\frac{\partial h}{\partial x}\right)^2\\
&\quad+\frac{qs's'''}{4}-qs'\frac{\partial^3 h}{\partial x^3}-q\frac{\partial h}{\partial x}s'''-3\frac{\partial h}{\partial x}\frac{\partial q}{\partial x}s''-\frac{9}{14}\left(\frac{\partial h}{\partial x}\right)^2\frac{\partial^2 q}{\partial x^2}+\frac{9\left(s'\right)^2}{4}\frac{\partial^2 q}{\partial x^2}\\
&\quad-\frac{11h^2}{56}\frac{\partial^4 q}{\partial x^4}-\frac{123q}{56}\left(\frac{\partial^2 h}{\partial x^2}\right)^2-\frac{3q\left(s''\right)^2}{4}+\frac{107h}{56}\frac{\partial^2 h}{\partial x^2}\frac{\partial^2 q}{\partial x^2}+\frac{5hs''}{2}\frac{\partial^2 q}{\partial x^2}+\frac{107h}{84}\frac{\partial q}{\partial x}\frac{\partial^3 h}{\partial x^3}\\
&\quad+\frac{5hs'''}{3}\frac{\partial q}{\partial x}+\frac{37h}{84}\frac{\partial h}{\partial x}\frac{\partial^3 q}{\partial x^3}+\frac{5hs'}{6}\frac{\partial^3 q}{\partial x^3}+\frac{107hq}{336}\frac{\partial^4 h}{\partial x^4}+\frac{5hqs''''}{12}+\frac{3s's''}{4}\frac{\partial q}{\partial x}\Big]\\
&\quad+\frac{5g}{(1-\varepsilon^2 g)}\left(\frac{\partial^2 q}{\partial x^2}-\frac{1}{2h}\frac{\partial q}{\partial x}\frac{\partial h}{\partial x}+\frac{q}{2h^2}\left(\frac{\partial h}{\partial x}\right)^2-\frac{q}{h}\frac{\partial^2 h}{\partial x^2}+\frac{3s'}{2h}\frac{\partial q}{\partial x}-\frac{3qs'}{2h^2}\frac{\partial h}{\partial x}\right)\\
&\quad+\frac{5h}{(1-\varepsilon^2 g)^2}\frac{\partial g}{\partial x}\frac{\partial}{\partial x}\left(\frac{q}{h}\right)\Big].
\end{aligned}
\tag{A.1}
$$

Appendix B Steady-State WIBL1-4 Models

Each individual model is obtained by cancelling terms of higher order.

$$
\begin{aligned}
-\frac{4\varepsilon Re}{7h_s^2}h_s' &= \frac{5h_s}{3} - \frac{5}{3h_s^2} - \frac{5h_s}{3}\varepsilon\cot\beta\,(h_s'+s') + \frac{5h\varepsilon^3}{6Ca}\Big[\frac{(h_s''+s'')}{(1+\varepsilon^2 g_s)^{3/2}}\Big]' \\
&+\varepsilon^2\Big[\frac{8\,(h_s')^2}{3h_s^2} - \frac{4h_s''}{h_s} - \frac{10\,(s')^2}{3h_s^2} - \frac{5s''}{2h_s} - \frac{5h_s's'}{3h_s^2}\Big] \\
+\varepsilon^3 Re\Big[&-\frac{73s'''}{288} - \frac{1205h_s'''}{6048} - \frac{115\,(h_s')^3}{1512h_s^2} + \frac{4h_s'\,(s')^2}{7h_s^2} + \frac{163\,(h_s')^2\,s'}{504h_s^2} \\
&+\frac{185h_s''h_s'}{672h_s} - \frac{4s's''}{7h_s} - \frac{163h_s''s'}{1008h_s} + \frac{185h_s's''}{2016h_s}\Big] \\
+\varepsilon^4\Big[&-\frac{2h_s's'''}{3} - \frac{47h_s'h_s'''}{42} - \frac{9h_s''s''}{4} + \frac{s's'''}{6} - \frac{10\,(h_s')^4}{21h_s^2} - \frac{2s'h_s'''}{3} \\
&-\frac{5\,(s')^4}{3h_s^2} + \frac{5h_s s''''}{18} + \frac{107h_s h_s''''}{504} + \frac{5h_s'\,(s')^3}{6h_s^2} + \frac{11\,(h_s')^2\,(s')^2}{2h_s^2} \\
&+\frac{8\,(h_s')^3\,s'}{3h_s^2} - \frac{15\,(s')^2\,s''}{4h_s} - \frac{13\,(s')^2\,h_s''}{4h_s} + \frac{(h_s')^2\,s''}{h_s} \\
&+\frac{22\,(h_s')^2\,h_s''}{7h_s} - \frac{41\,(h_s'')^2}{28} - \frac{(s'')^2}{2} - \frac{4h_s's's''}{h_s} - \frac{h_s's'h_s''}{2h_s} \\
&+\frac{5g_s}{(1-\varepsilon^2 g_s)}\left(\frac{(h_s')^2}{3h_s^2} - \frac{2h_s''}{3h_s} - \frac{s'h_s'}{h_s^2}\right) - \frac{10g_s'h_s'}{3h_s\,(1-\varepsilon^2 g_s)^2}\Big].
\end{aligned}
\tag{B.1}
$$

Appendix C Coefficients of Linearised Perturbation Equations for WIBL1-4 models

Each individual model is obtained by cancelling terms of higher order.

$$
\begin{aligned}
\alpha_0(x) &= \varepsilon Re + \varepsilon^3 Re\Big[\frac{5hs''}{12} + (s')^2 + \frac{29\,(h_s')^2}{56} + \frac{11h_s's'}{8} + \frac{107hh_s''}{336}\Big],\\
\alpha_1(x) &= -\varepsilon^3 Re\frac{11hh_s'}{56},\\
\alpha_2(x) &= -\varepsilon^3 Re\frac{11h_s^2}{56},
\end{aligned}
\tag{C.1}
$$

$$
\begin{aligned}
\beta_0(x) = {}& \frac{8h_s'}{7h_s^3}\varepsilon Re - \frac{5}{3} - \frac{10}{3h_s^3} + \frac{5}{3}\varepsilon\cot\beta\,(h_s' + s') - \frac{5\varepsilon^3}{6Ca}\Big[\frac{(h_s'' + s'')}{(1+\varepsilon^2 g_s)^{3/2}}\Big]'\\
&+ \varepsilon^2\Big[-\frac{20\,(s')^2}{3h_s^3} + \frac{16\,(h_s')^2}{3h_s^3} - \frac{4h_s''}{h_s^2} - \frac{5s''}{2h_s^2} - \frac{10h_s's'}{3h_s^3}\Big]\\
&+ \varepsilon^3 Re\Big[\frac{185s''h_s'}{2016h_s^2} - \frac{4s's''}{7h_s^2} - \frac{163s'h_s''}{1008h_s^2} + \frac{185h_s''h_s'}{672h_s^2} - \frac{115\,(h_s')^3}{756h_s^3} + \frac{8h_s'\,(s')^2}{7h_s^3} + \frac{163\,(h_s')^2\,s'}{252h_s^3}\Big]\\
&+ \varepsilon^4\Big[-\frac{5s''''}{18} - \frac{4s's''h_s'}{h_s^2} - \frac{15\,(s')^2\,s''}{4h_s^2} + \frac{22h_s''\,(h_s')^2}{7h_s^2} - \frac{13h_s''\,(s')^2}{4h_s^2} - \frac{10\,(s')^4}{3h_s^3}\\
&- \frac{20\,(h_s')^4}{21h_s^3} - \frac{107h_s''''}{504} - \frac{h_s''h_s's'}{2h_s^2} + \frac{(h_s')^2\,s''}{h_s^2} + \frac{11\,(h_s')^2\,(s')^2}{h_s^3} + \frac{5h_s'\,(s')^3}{3h_s^3} + \frac{16\,(h_s')^3\,s'}{3h_s^3}\\
&+ \frac{5g_s}{(1-\varepsilon^2 g_s)}\left(\frac{2\,(h_s')^2}{3h_s^3} - \frac{2h_s''}{3h_s^2} - \frac{2s'h_s'}{h_s^3}\right) - \frac{10h_s'g_s'}{3h_s^2\,(1-\varepsilon^2 g_s)^2}\Big],\\
\beta_1(x) = {}& -\frac{4}{7h_s^2}\varepsilon Re + \frac{5h\varepsilon\cot\beta}{3} + \frac{15h\varepsilon^5}{12Ca}\Big[\frac{g_s'}{(1+\varepsilon^2 g_s)^{5/2}}\Big]' + \varepsilon^2\Big[\frac{5s'}{3h_s^2} - \frac{16h_s'}{3h_s^2}\Big] + \varepsilon^3 Re\Big[\frac{115\,(h_s')^2}{504h_s^2}\\
&- \frac{185s''}{2016h} - \frac{185h_s''}{672h} - \frac{4\,(s')^2}{7h_s^2} - \frac{163s'h_s'}{252h_s^2}\Big] + \varepsilon^4\Big[\frac{47h_s'''}{42} - \frac{2s''h_s'}{h} - \frac{44h_s'h_s''}{7h} + \frac{4s's''}{h} + \frac{s'h_s''}{2h}\\
&- \frac{5\,(s')^3}{6h_s^2} + \frac{40\,(h_s')^3}{21h_s^2} - \frac{8s'\,(h_s')^2}{h_s^2} + \frac{2s'''}{3} - \frac{11\,(s')^2\,h_s'}{h_s^2} + \frac{5g_s}{(1-\varepsilon^2 g_s)}\left(\frac{s'}{h_s^2} - \frac{2h_s'}{3h_s^2}\right)\\
&+ \frac{10\,(h_s' + s')}{(1-\varepsilon^2 g_s)^2}\left(\frac{2h_s''}{3h_s} + \frac{s'h_s'}{h_s^2} - \frac{(h_s')^2}{3h_s^2}\right) + \frac{20\,(h_s'' + s'')\,[2h_s' + s' + \varepsilon^2 g_s\,(2h_s' - s')]}{3h_s\,(1-\varepsilon^2 g_s)^3}\Big],\\
\beta_2(x) = {}& \frac{5hg_s'\varepsilon^5}{2Ca\,(1+\varepsilon^2 g_s)^{5/2}} + \frac{4}{h}\varepsilon^2 + \varepsilon^3 Re\Big[\frac{163s'}{1008h} - \frac{185h_s'}{672h}\Big] + \varepsilon^4\Big[\frac{41h_s''}{14} + \frac{h_s's'}{2h}\\
&+ \frac{9s''}{4} - \frac{22\,(h_s')^2}{7h} + \frac{13\,(s')^2}{4h} + \frac{10}{3h_s}\left(\frac{g_s}{(1-\varepsilon^2 g_s)} + \frac{2\,(h_s' + s')\,h_s'}{(1-\varepsilon^2 g_s)^2}\right)\Big],\\
\beta_3(x) = {}& -\frac{5h\varepsilon^3}{6Ca\,(1+\varepsilon^2 g_s)^{3/2}} + \frac{1205}{6048}\varepsilon^3 Re + \varepsilon^4\Big[\frac{2s'}{3} + \frac{47h_s'}{42}\Big],\\
\beta_4(x) = {}& -\varepsilon^4\frac{107h}{504},
\end{aligned}
\tag{C.2}
$$

$$
\begin{aligned}
\gamma_0(x) &= \frac{5}{2h_s^2} - \frac{12h_s'}{7h_s^2}\varepsilon Re + \varepsilon^2\Big[\frac{5h_s's'}{2h_s^2} - \frac{4\left(h_s'\right)^2}{h_s^2} + \frac{5\left(s'\right)^2}{h_s^2} + \frac{6h_s''}{h_s} + \frac{15s''}{4h_s}\Big] \\
&+ \varepsilon^3 Re\Big[\frac{163h_s''s'}{336h_s} - \frac{\left(h_s'\right)^2 s'}{168h_s^2} - \frac{185h_s''h_s'}{224h_s} + \frac{12s's''}{7h_s} - \frac{185h_s's''}{672h_s} - \frac{12h_s'\left(s'\right)^2}{7h_s^2} \\
&+ \frac{73s'''}{96} + \frac{1205h_s'''}{2016} + \frac{115\left(h_s'\right)^3}{504h_s^2}\Big] + \varepsilon^4\Big[\frac{3\left(s''\right)^2}{4} + \frac{3h_s''h_s's'}{4h_s} + \frac{6h_s's's''}{h_s} + h_s's''' \\
&+ s'h_s''' + \frac{47h_s'h_s'''}{28} + \frac{45\left(s'\right)^2 s''}{8h_s} - \frac{3\left(h_s'\right)^2 s''}{2h_s} - \frac{33h_s''\left(h_s'\right)^2}{7h_s} + \frac{39h_s''\left(s'\right)^2}{8h_s} + \frac{27h_s''s''}{8} - \frac{5h_s'\left(s'\right)^3}{4h_s^2} \\
&- \frac{4\left(h_s'\right)^3 s'}{h_s^2} - \frac{33\left(h_s'\right)^2\left(s'\right)^2}{4h_s^2} - \frac{s's'''}{4} + \frac{5\left(s'\right)^4}{2h_s^2} + \frac{5\left(h_s'\right)^4}{7h_s^2} - \frac{107h_sh_s''''}{336} - \frac{5s''''h_s}{12} + \frac{123\left(h_s''\right)^2}{56} \\
&+ \frac{5g_s}{\left(1-\varepsilon^2 g_s\right)}\left(\frac{h_s''}{h_s} - \frac{\left(h_s'\right)^2}{2h_s^2} + \frac{3s'h_s'}{2h_s^2}\right) + \frac{5h_s'g_s'}{h_s\left(1-\varepsilon^2 g_s\right)^2}\Big], \\
\gamma_1(x) &= \frac{34\varepsilon Re}{21h_s} + \varepsilon^2\frac{9h_s'}{2h_s} + \varepsilon^3 Re\Big[\frac{34\left(s'\right)^2}{21h_s} - \frac{253\left(h_s'\right)^2}{1008h_s} + \frac{4633h_s''}{4032} + \frac{99s'h_s'}{112h_s} + \frac{277s''}{192}\Big] \\
&+ \varepsilon^4\Big[\frac{15\left(s'\right)^3}{4h_s} + \frac{39h_s'\left(s'\right)^2}{4h_s} + \frac{9\left(h_s'\right)^2 s'}{2h_s} + 3h_s''s' + h_s's'' + \frac{141h_s'h_s''}{28} - \frac{107h_sh_s'''}{84} \\
&- \frac{9\left(h_s'\right)^3}{14h_s} - \frac{5hs'''}{3} - \frac{3s's''}{4} + \frac{5g_s}{\left(1-\varepsilon^2 g_s\right)}\left(\frac{h_s'}{2h_s} - \frac{3s'}{2h_s}\right) - \frac{5g_s'}{\left(1-\varepsilon^2 g_s\right)^2}\Big], \\
\gamma_2(x) &= -\frac{9}{2}\varepsilon^2 - \varepsilon^3 Re\Big[\frac{187h_s'}{2016} + \frac{5s'}{32}\Big] - \varepsilon^4\Big[\frac{9\left(s'\right)^2}{4} + \frac{3h_s's'}{4} + \frac{5hs''}{2} + \frac{107hh_s''}{56} - \frac{9\left(h_s'\right)^2}{14} \\
&- \frac{5g_s}{\left(1-\varepsilon^2 g_s\right)}\Big], \\
\gamma_3(x) &= -\varepsilon^3 Re\frac{601h}{1512} - \varepsilon^4\Big[\frac{37hh_s'}{84} + \frac{5hs'}{6}\Big], \\
\gamma_4(x) &= \varepsilon^4\frac{11h_s^2}{56}.
\end{aligned}
\tag{C.3}
$$

Figures

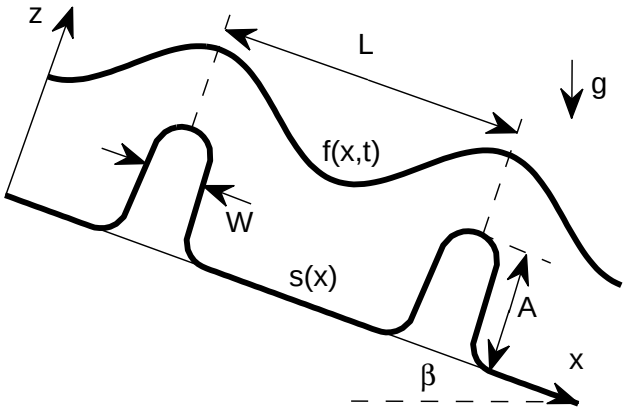

Figure 1: Schematic of film flow over inclined substrate containing smooth periodic rectangular corrugations.

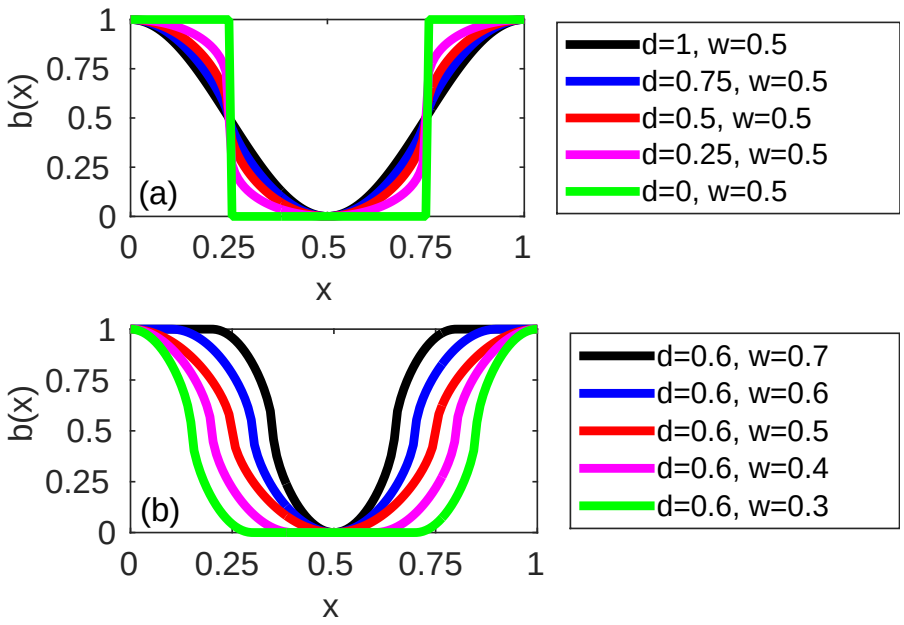

Figure 2: Profiles of smoothed rectangular corrugations for (a) variation of steepness for constant tip width and (b) variation of tip width with the steepness held constant.

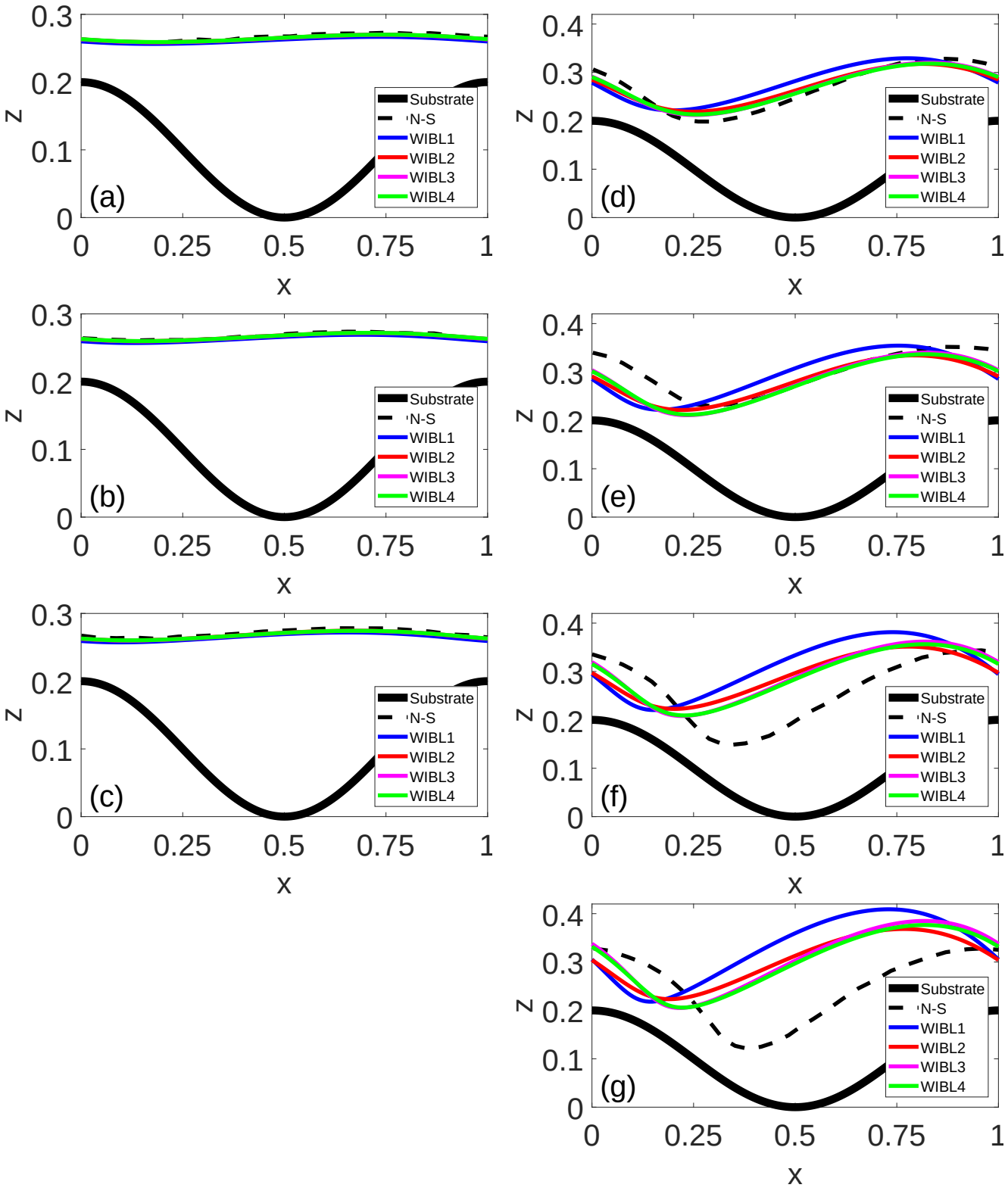

Figure 3: WIBL1-4 generated steady-state free surface profiles for films flowing over a sinusoidally varying substrate compared with (left column) Fig. 5 and (right column) Fig. 6 from Nguyen and Bontozoglou [17] obtained for $\beta = 45°$, $A/L = 0.2$, (a-c) $L/L_c = 1.057$, $Re = 7.5, 15, 22.5$, $Ka = 5.937, 6.735, 7.250$ and (d-g) $L/L_c = 3.342$, $Re = 15, 22.5, 30, 37.5$, $Ka = 3.594, 3.869, 4.077, 4.246$.

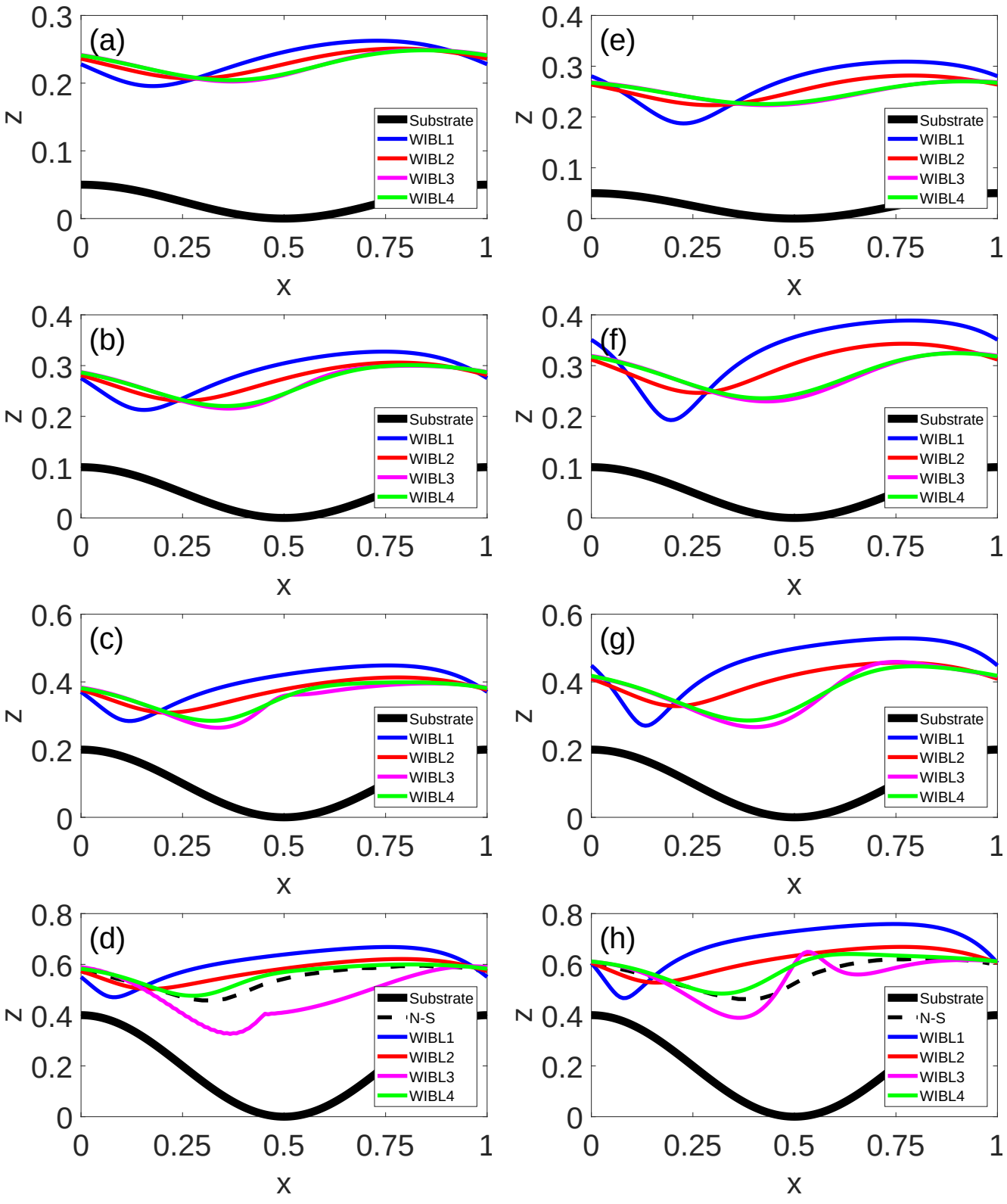

Figure 4: WIBL1-4 generated steady-state free surface profiles for films flowing over a sinusoidally varying substrate compared with Fig. 9 from Trifonov [41] obtained for $Ka = 1.434$, $L/L_c = 13.746$, $\beta = 10°$, (a-d) $Re = 12.75$ and (e-h) $Re = 17.55$ for (top to bottom) $A/L = 0.05, 0.1, 0.2, 0.4$.

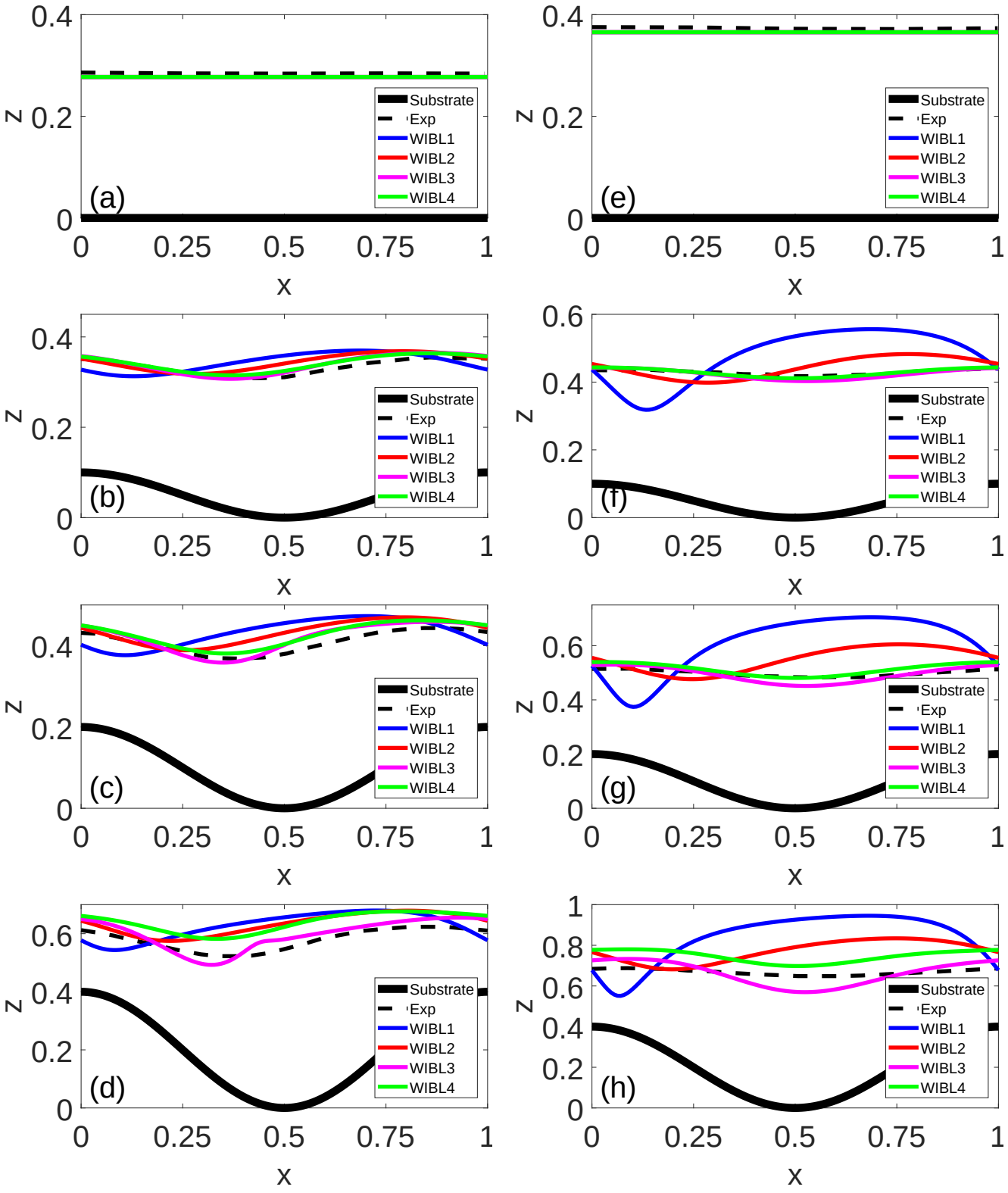

Figure 5: WIBL1-4 generated steady-state free surface profiles for films flowing over a sinusoidally varying substrate compared with Fig. 8 from Schörner et al. [35] obtained for $Ka = 1.069$, $L/L_c = 13.741$, $\beta = 10°$, (a-d) $Re = 7.0$ and (e-h) $Re = 16.0$ for (top to bottom) $A/L = 0.05, 0.1, 0.2, 0.4$.

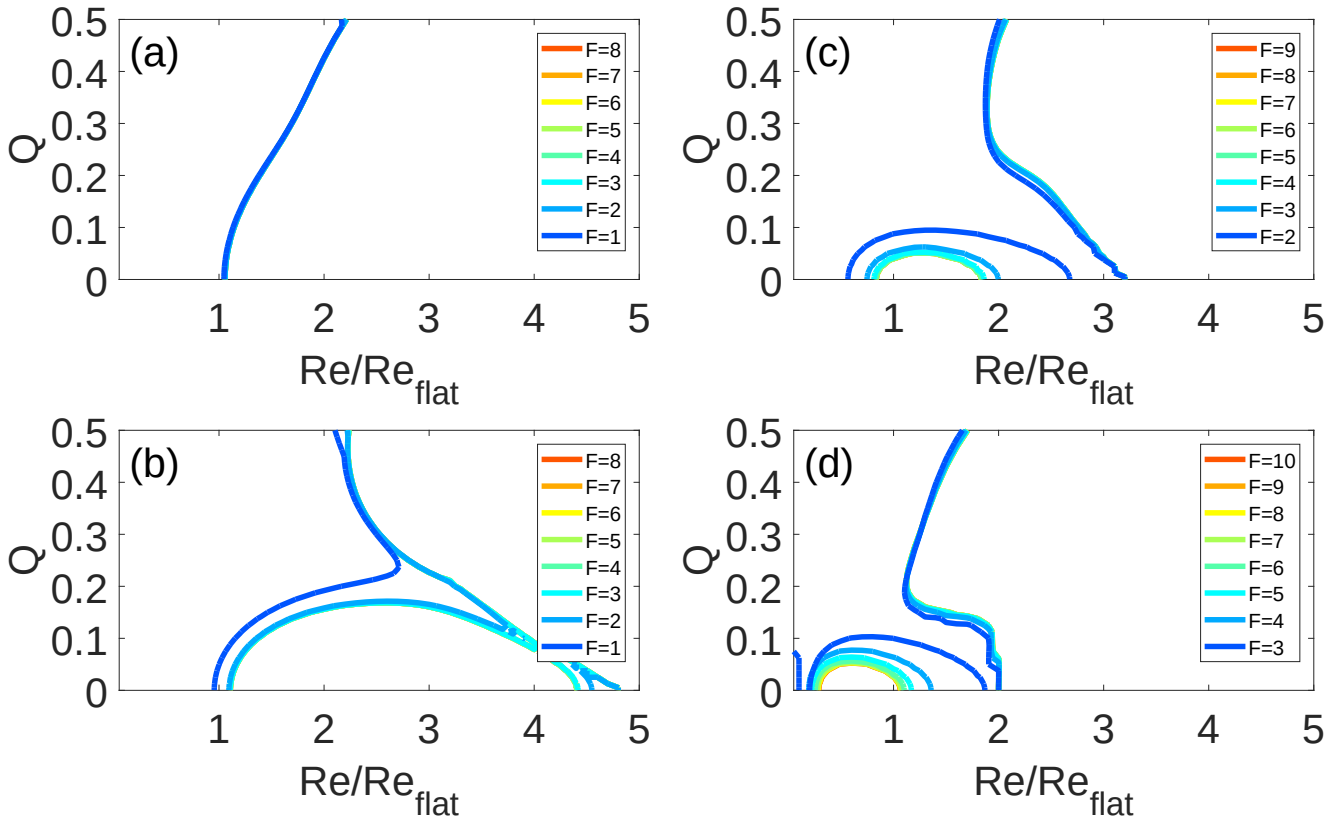

Figure 6: WIBL2 generated curves of neutral disturbance in the Floquet domain $(Re/Re_{flat}, Q)$ for films flowing over a sinusoidally varying substrate of Fig. 1 from Trifonov [42] showing the effect of the number of Floquet harmonics F for $\beta = 10°$, $Ka = 10$, $L/L_c = 3$, (a-d) $A/L = 0.01, 0.02, 0.04, 0.08$.

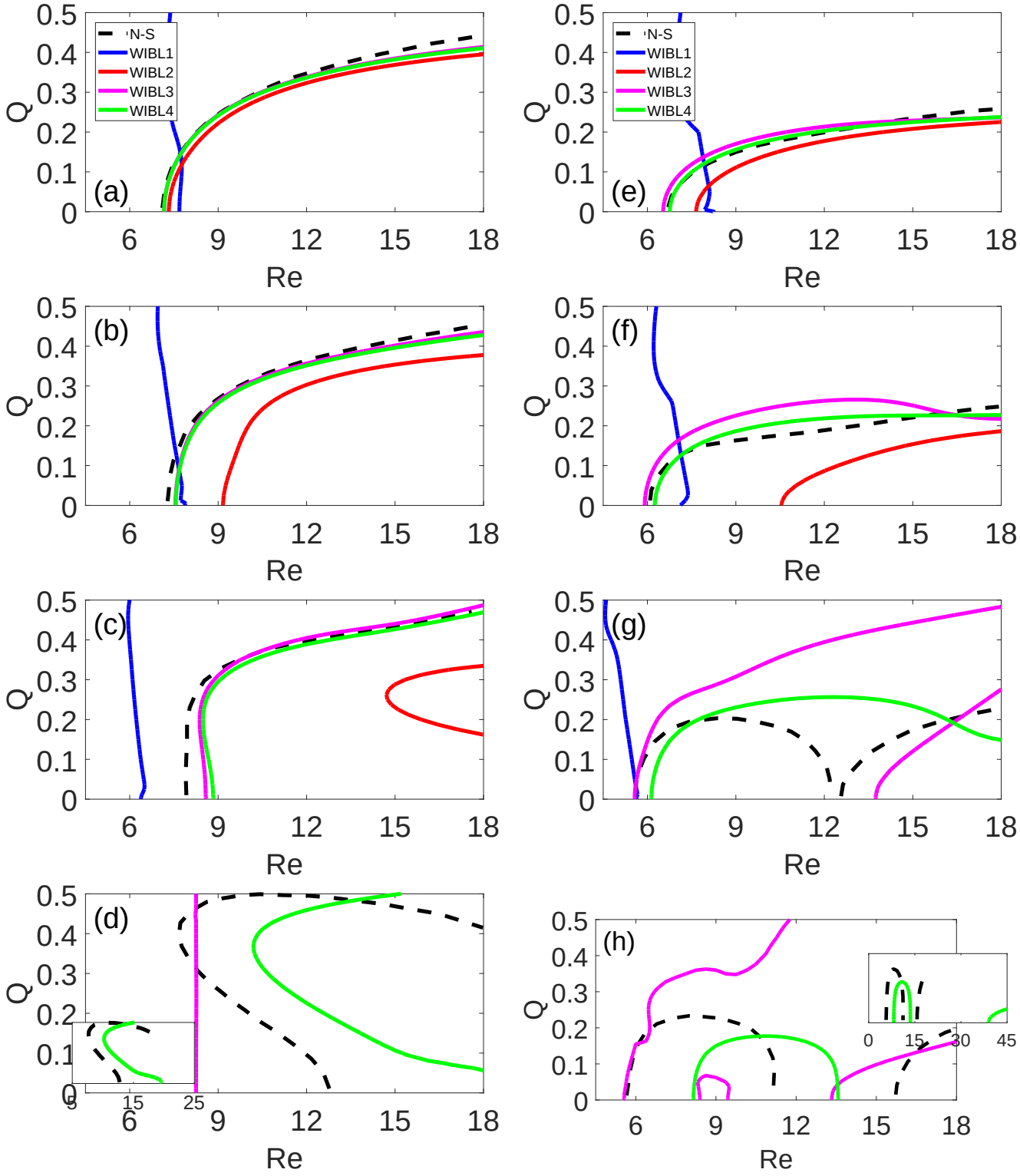

Figure 7: WIBL1-4 generated curves of neutral disturbance in the Floquet domain (Re, Q) for films flowing over a sinusoidally varying substrate compared with (left column) Fig. 3a and (right column) Fig. 3a' from Trifonov [41] obtained for $\beta = 10°$, (a-d) $Ka = 1.434$, $L/L_c = 13.746$, $A/L = 0.02, 0.05, 0.1, 0.4$ and (e-h) $Ka = 1.069$, $L/L_c = 13.741$, $A/L = 0.05, 0.1, 0.2, 0.4$. Insets in bottom figures of both columns show extended range for WIBL4 results.

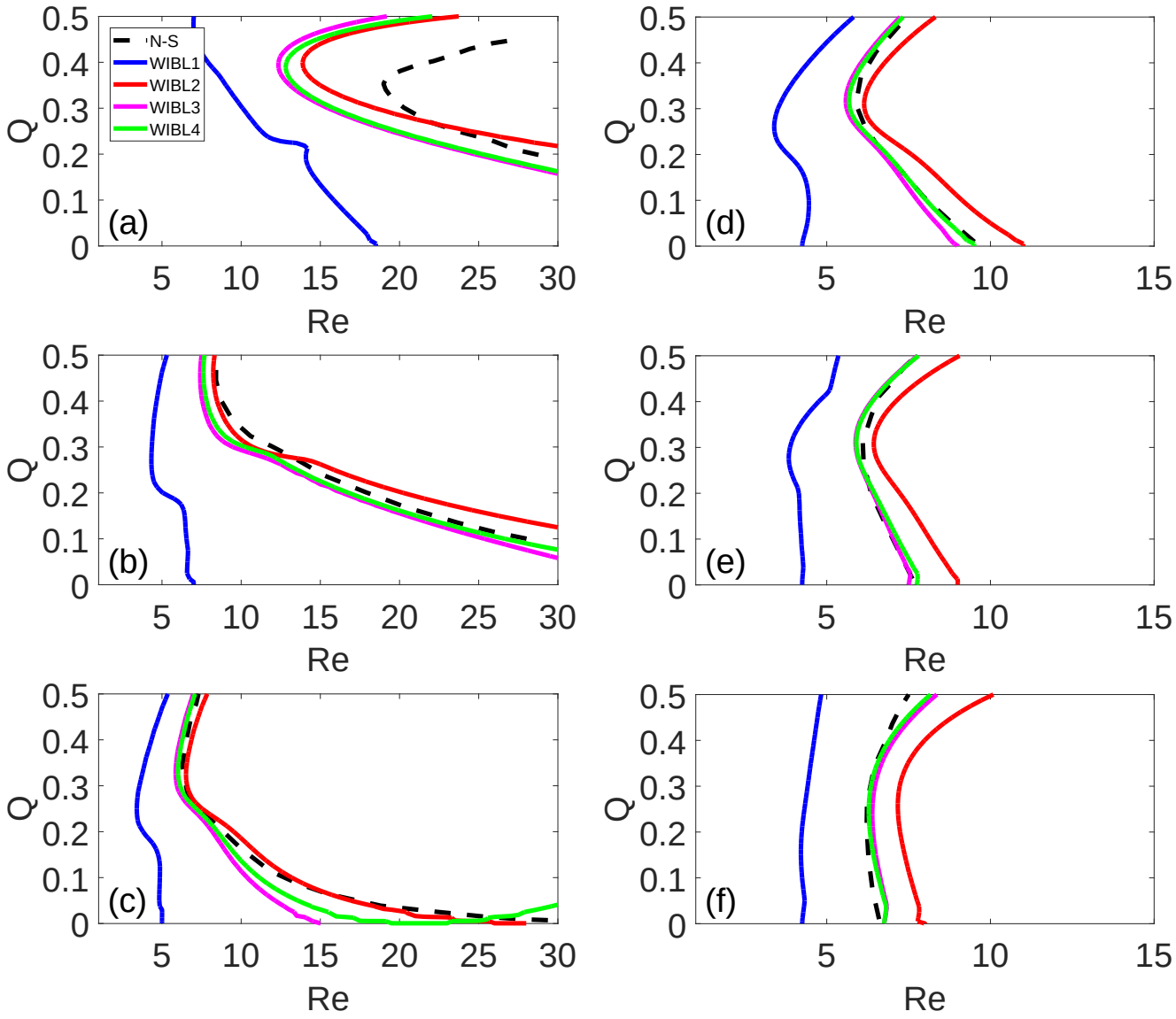

Figure 8: WIBL1-4 generated curves of neutral disturbance in the Floquet domain (Re, Q) for films flowing over a sinusoidally varying substrate compared with Fig. 8c from Schörner et al. [46] obtained for $Ka = 3.604$, $L/L_c = 4.982$, $A/L = 0.167$ and (a-f) $\beta = 5, 10, 15, 20, 25, 35°$.

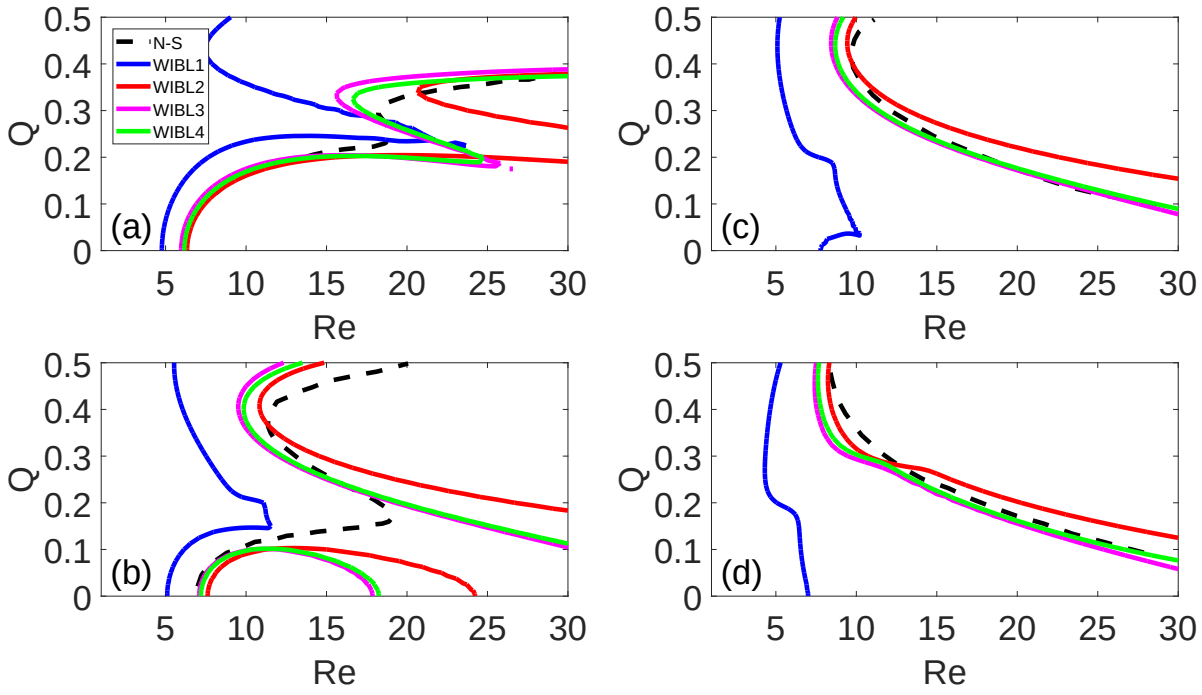

Figure 9: WIBL1-4 generated curves of neutral disturbance in the Floquet domain (Re, Q) for films flowing over a sinusoidally varying substrate compared with Fig. 9a from Schörner et al. [46] obtained for $Ka = 3.604$, $A/L = 0.167$, $\beta = 10°$ and (a-d) $L/L_c = 2.5, 3.5, 4.0, 4.9$.

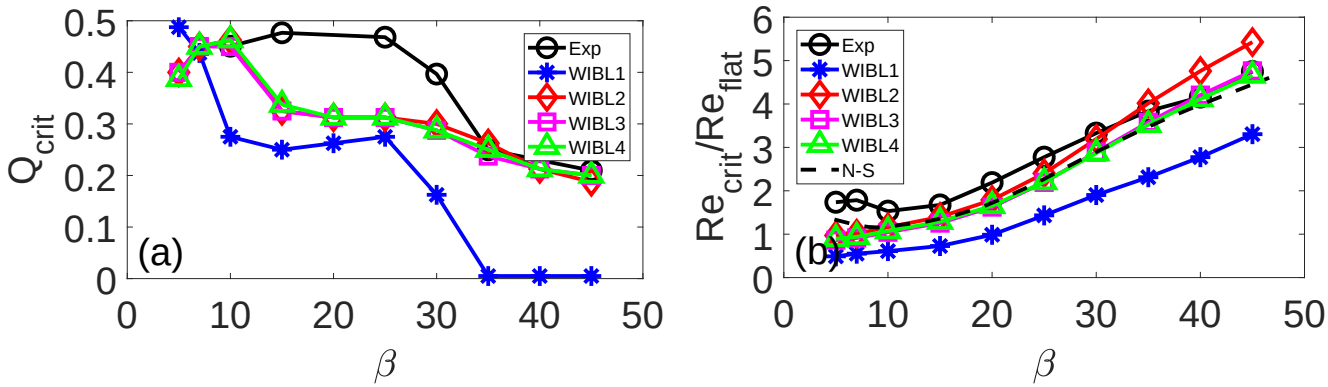

Figure 10: Comparison of the experimental results of Cao et al. and the N-S results of Schörner et al. with results from WIBL1-4 for $Ka = 3.604$, $L/L_c = 4.982$, $A/L = 0.167$: (a) critical Floquet parameter vs angle of inclination (Fig. 10 from [30]) and (b) normalised critical Reynolds number vs angle of inclination (Fig. 12 from [30] and Fig. 8d N-S Variant 1b from [46]).

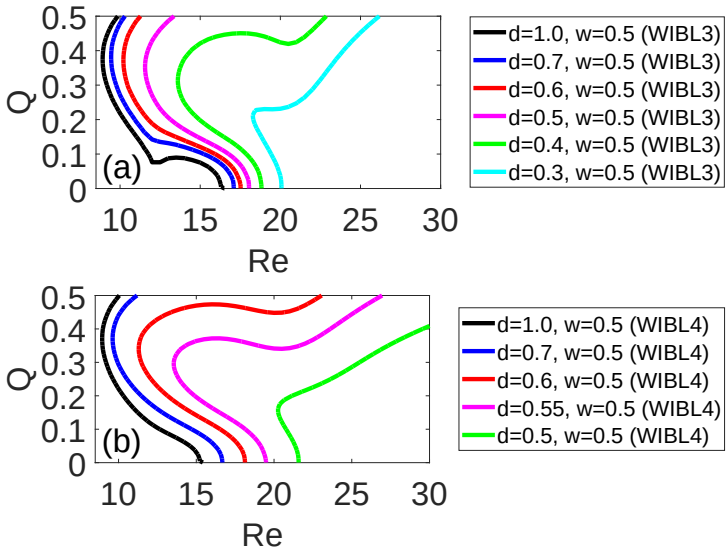

Figure 11: WIBL3-4 generated curves of neutral disturbance in the Floquet domain (Re, Q) for films flowing over wall with smoothed rectangular corrugation for $Ka = 1.223$, $A/L = 0.1$, $\beta = 10°$, $L/L_c = 27.446$, $w = 0.5$, (a) WIBL3 and (b) WIBL4.

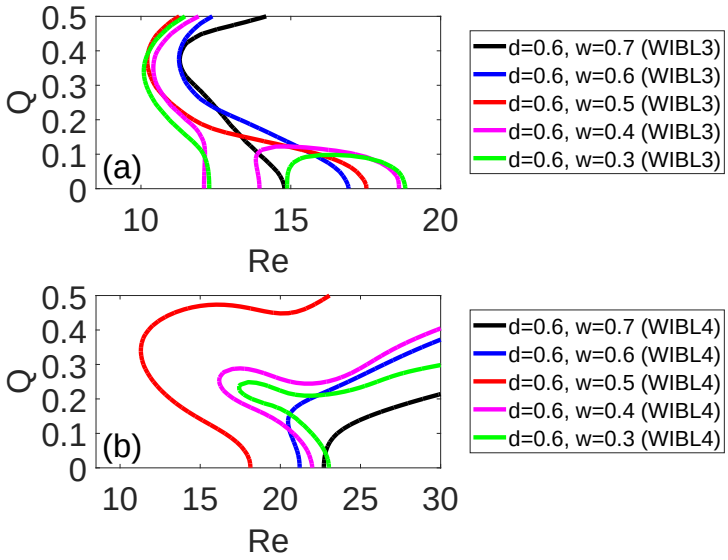

Figure 12: WIBL3-4 generated curves of neutral disturbance in the Floquet domain (Re, Q) for films flowing over wall with smoothed rectangular corrugation for $Ka = 1.223$, $A/L = 0.1$, $\beta = 10°$, $L/L_c = 27.446$, $d = 0.6$, (a) WIBL3 and (b) WIBL4.

References

[1] S. F. Kistler and P. M. Schweizer, *Liquid film coating*. Chapman & Hall, 1997.

[2] F. C. Krebs, "Roll-to-roll fabrication of monolithic large-area polymer solar cells free from indium-tin-oxide," *Solar Energy Materials and Solar Cells*, vol. 93, no. 9, pp. 1636 – 1641, 2009.

[3] B. Kang, W. H. Lee, and K. Cho, "Recent advances in organic transistor printing processes," *ACS applied materials & interfaces*, vol. 5, no. 7, pp. 2302–2315, 2013.

[4] C. D. Müller, A. Falcou, N. Reckefuss, M. Rojahn, V. Wiederhirn, P. Rudati, H. Frohne, O. Nuyken, H. Becker, and K. Meerholz, "Multi-colour organic light-emitting displays by solution processing," *Nature*, vol. 421, no. 6925, pp. 829–833, 2003.

[5] S. Mandal, G. Dell'Erba, A. Luzio, S. G. Bucella, A. Perinot, A. Calloni, G. Berti, G. Bussetti, L. Duò, A. Facchetti, Y.-Y. Noh, and M. Caironi, "Fully-printed, all-polymer, bendable and highly transparent complementary logic circuits," *Organic Electronics*, vol. 20, pp. 132–141, 2015.

[6] T. Someya, T. Sekitani, S. Iba, Y. Kato, H. Kawaguchi, and T. Sakurai, "A large-area, flexible pressure sensor matrix with organic field-effect transistors for artificial skin applications," *Proceedings of the National Academy of Sciences of the United States of America*, vol. 101, no. 27, pp. 9966–9970, 2004.

[7] L. Cao, A. K. Jones, V. K. Sikka, J. Wu, and D. Gao, "Anti-icing superhydrophobic coatings," *Langmuir*, vol. 25, no. 21, pp. 12444–12448, 2009.

[8] M. Scholle, A. Rund, and N. Aksel, "Drag reduction and improvement of material transport in creeping films," *Archive of Applied Mechanics*, vol. 75, no. 2-3, pp. 93–112, 2006.

[9] K. Jakab, C. Norotte, F. Marga, K. Murphy, G. Vunjak-Novakovic, and G. Forgacs, "Tissue engineering by self-assembly and bio-printing of living cells," *Biofabrication*, vol. 2, no. 2, p. 022001, 2010.

[10] R. V. Craster and O. K. Matar, "Dynamics and stability of thin liquid films," *Reviews of Modern Physics*, vol. 81, pp. 1131–1198, Aug 2009.

[11] N. Aksel and M. Schörner, "Films over topography: From creeping flow to linear stability, theory, and experiments, a review," *Acta Mechanica*, vol. 229, no. 4, pp. 1453–1482, 2018.

[12] V. Bontozoglou, "Laminar film flow along a periodic wall," *CMES(Computer Modelling in Engineering & Sciences)*, vol. 1, no. 2, pp. 133–142, 2000.

[13] A. Wierschem, M. Scholle, and N. Aksel, "Comparison of different theoretical approaches to experiments on film flow down an inclined wavy channel," *Experiments in Fluids*, vol. 33, no. 3, pp. 429–442, 2002.

[14] M. Scholle, A. Wierschem, and N. Aksel, "Creeping films with vortices over strongly undulated bottoms," *Acta Mechanica*, vol. 168, no. 3-4, pp. 167–193, 2004.

[15] A. Wierschem and N. Aksel, "Influence of inertia on eddies created in films creeping over strongly undulated substrates," *Physics of Fluids*, vol. 16, no. 12, pp. 4566–4574, 2004.

[16] M. Scholle, A. Haas, N. Aksel, M. C. T. Wilson, H. M. Thompson, and P. H. Gaskell, "Competing geometric and inertial effects on local flow structure in thick gravity-driven fluid films," *Physics of Fluids*, vol. 20, no. 12, p. 123101, 2008.

[17] P.-K. Nguyen and V. Bontozoglou, "Steady solutions of inertial film flow along strongly undulated substrates," *Physics of Fluids*, vol. 23, no. 5, p. 052103, 2011.

[18] M. I. Pak and G. H. Hu, "Numerical investigations on vortical structures of viscous film flows along periodic rectangular corrugations," *International Journal of Multiphase Flow*, vol. 37, no. 4, pp. 369–379, 2011.

[19] S. Veremieiev, H. M. Thompson, and P. H. Gaskell, "Free-surface film flow over topography: Full three-dimensional finite element solutions," *Computers & Fluids*, vol. 122, pp. 66–82, 2015.

[20] A. Wierschem and N. Aksel, "Hydraulic jumps and standing waves in gravity-driven flows of viscous liquids in wavy open channels," *Physics of Fluids*, vol. 16, no. 11, pp. 3868–3877, 2004.

[21] A. Wierschem, V. Bontozoglou, C. Heining, H. Uecker, and N. Aksel, "Linear resonance in viscous films on inclined wavy planes," *International Journal of Multiphase Flow*, vol. 34, no. 6, pp. 580–589, 2008.

[22] C. Heining, V. Bontozoglou, N. Aksel, and A. Wierschem, "Nonlinear resonance in viscous films on inclined wavy planes," *International Journal of Multiphase Flow*, vol. 35, no. 1, pp. 78–90, 2009.

[23] S. V. Alekseenko, V. E. Nakoryakov, and B. G. Pokusaev, *Wave Flow in Liquid Films*. Begell House, New York, 1994.

[24] T. B. Benjamin, "Wave formation in laminar flow down an inclined plane," *Journal of Fluid Mechanics*, vol. 2, no. 6, p. 554–573, 1957.

[25] C. S. Yih, "Stability of liquid flow down an inclined plane," *Physics of Fluids*, vol. 6, no. 3, pp. 321–334, 1963.

[26] M. Vlachogiannis and V. Bontozoglou, "Experiments on laminar film flow along a periodic wall," *Journal of Fluid Mechanics*, vol. 457, pp. 133–156, 2002.

[27] A. Wierschem and N. Aksel, "Instability of a liquid film flowing down an inclined wavy plane," *Physica D: Nonlinear Phenomena*, vol. 186, no. 3, pp. 221 – 237, 2003.

[28] A. Wierschem, C. Lepski, and N. Aksel, "Effect of long undulated bottoms on thin gravity-driven films," *Acta Mechanica*, vol. 179, no. 1-2, pp. 41–66, 2005.

[29] K. Argyriadi, M. Vlachogiannis, and V. Bontozoglou, "Experimental study of inclined film flow along periodic corrugations: The effect of wall steepness," *Physics of Fluids*, vol. 18, no. 1, p. 012102, 2006.

[30] Z. Cao, M. Vlachogiannis, and V. Bontozoglou, "Experimental evidence for a short-wave global mode in film flow along periodic corrugations," *Journal of Fluid Mechanics*, vol. 718, p. 304–320, 2013.

[31] T. Pollak and N. Aksel, "Crucial flow stabilization and multiple instability branches of gravity-driven films over topography," *Physics of Fluids*, vol. 25, no. 2, p. 024103, 2013.

[32] M. Schörner, D. Reck, and N. Aksel, "Does the topography's specific shape matter in general for the stability of film flows?," *Physics of Fluids*, vol. 27, no. 4, p. 042103, 2015.

[33] M. Schörner and N. Aksel, "The stability cycle—a universal pathway for the stability of films over topography," *Physics of Fluids*, vol. 30, no. 1, p. 012105, 2018.

[34] Y. Y. Trifonov, "Stability of a viscous liquid film flowing down a periodic surface," *International Journal of Multiphase Flow*, vol. 33, no. 11, pp. 1186–1204, 2007.

[35] M. Schörner, D. Reck, and N. Aksel, "Stability phenomena far beyond the nusselt flow – revealed by experimental asymptotics," *Physics of Fluids*, vol. 28, no. 2, p. 022102, 2016.

[36] L. A. Dávalos-Orozco, "Nonlinear instability of a thin film flowing down a smoothly deformed surface," *Physics of Fluids*, vol. 19, no. 7, p. 074103, 2007.

[37] T. Häcker and H. Uecker, "An integral boundary layer equation for film flow over inclined wavy bottoms," *Physics of Fluids*, vol. 21, no. 9, p. 092105, 2009.

[38] S. J. D. D'Alessio, J. P. Pascal, and H. A. Jasmine, "Instability in gravity-driven flow over uneven surfaces," *Physics of Fluids*, vol. 21, no. 6, p. 062105, 2009.

[39] S. Veremieiev, H. M. Thompson, Y. C. Lee, and P. H. Gaskell, "Inertial thin film flow on planar surfaces featuring topography," *Computers & Fluids*, vol. 39, no. 3, pp. 431–450, 2010.

[40] D. Tseluiko, M. G. Blyth, and D. T. Papageorgiou, "Stability of film flow over inclined topography based on a long-wave nonlinear model," *Journal of Fluid Mechanics*, vol. 729, pp. 638–671, 2013.

[41] Y. Trifonov, "Stability of a film flowing down an inclined corrugated plate: The direct navier-stokes computations and floquet theory," *Physics of Fluids*, vol. 26, no. 11, p. 114101, 2014.

[42] Y. Y. Trifonov, "Viscous liquid film flow down an inclined corrugated surface. calculation of the flow stability to arbitrary perturbations using an integral method," *Journal of Applied Mechanics and Technical Physics*, vol. 57, no. 2, pp. 195–201, 2016.

[43] V. Y. Shkadov, "Wave flow regimes of a thin layer of viscous fluid subject to gravity," *IRS Fluid Dynamics*, vol. 2, no. 1, pp. 29–34, 1967.

[44] C. Ruyer-Quil and P. Manneville, "Modeling film flows down inclined planes," *The European Physical Journal B-Condensed Matter and Complex Systems*, vol. 6, no. 2, pp. 277–292, 1998.

[45] C. Ruyer-Quil and P. Manneville, "Improved modeling of flows down inclined planes," *The European Physical Journal B-Condensed Matter and Complex Systems*, vol. 15, no. 2, pp. 357–369, 2000.

[46] M. Schörner, D. Reck, N. Aksel, and Y. Trifonov, "Switching between different types of stability isles in films over topographies," *Acta Mechanica*, vol. 229, no. 2, pp. 423–436, 2018.

[47] A. A. Nepomnyashchy, P. Colinet, and M. G. Velarde, *Interfacial phenomena and convection*. Chapman & Hall, 2001.